

DYNAMICAL SIMULATION OF NUCLEAR “PASTA”: SOFT CONDENSED MATTER IN DENSE STARS

Gentaro Watanabe^{a,b} and Hidetaka Sonoda^{c,b}*

^aNORDITA, Blegdamsvej 17, DK-2100 Copenhagen Ø, Denmark

^bThe Institute of Chemical and Physical Research (RIKEN)
Saitama 351-0198, Japan

^cDepartment of Physics, University of Tokyo, Tokyo 113-0033, Japan

Abstract

More than twenty years ago, it was predicted that nuclei can adopt interesting shapes, such as rods or slabs, etc., in the cores of supernovae and the crusts of neutron stars. These non-spherical nuclei are referred to as nuclear “pasta.”

In recent years, we have been studying the dynamics of the pasta phases using a method called quantum molecular dynamics (QMD) and have opened up a new aspect of study for this system. Our findings include: dynamical formation of the pasta phases by cooling down the hot uniform nuclear matter; phase diagrams in the density versus temperature plane; structural transitions between the pasta phases induced by compression and elucidation of the mechanism by which they proceed. In the present article, we give an overview of the basic physics and astrophysics of the pasta phases and review our works for readers in other fields.

1 Introduction

Massive stars with masses $M = 8 - (30 - 50)M_{\odot}$ (M_{\odot} is the mass of the sun) end their lives in the most spectacular and violent events in the Universe: explosions called supernovae, which are driven by gravitational collapse of the stellar core (see, e.g., Ref. [57]). The mechanism for the collapse-driven supernova explosion has been a central mystery in astrophysics for almost half a century [12].

Great efforts have been made to unravel the mystery and a qualitative picture has been obtained so far (see, e.g., Refs. [6, 25, 60, 71, 72, 73]). We now know that after supernova explosions the collapsing core becomes a dense compact object, neutron star, for

*Present address: CNR-INFM BEC Center, Department of Physics, University of Trento, Via Sommarive 14, 38050 Povo (TN) Italy

$M = 8 - 30M_{\odot}$ or further collapses to a black hole for $M \gtrsim 30M_{\odot}$. However, no calculations incorporating reasonable physical input succeeded in reproducing an explosion; in the calculations, shock waves stall on their way out of the collapsing core and the core does not explode but contracts into a black hole. These earlier studies suggest that interactions between neutrinos from the central region of the star and the shocked matter are important for the success of an explosion. This will hopefully revive the shock wave, and lead to a successful explosion.

In equilibrium dense matter in supernova cores and neutron stars, the existence of nuclei with rod-like and slab-like shape is predicted [20, 53]. Such nuclei with exotic shapes are referred to as nuclear ‘‘pasta.’’ The nuclear pasta itself is an interesting subject from the point of view of materials science of dense stellar matter and it has been studied by nuclear physicists in addition to astrophysicists for more than twenty years. Furthermore, the pasta phases have recently begun to attract the attention of many researchers (see, e.g., Refs. [9, 36] and references therein). As has been pointed out in Refs. [56, 65, 67] and elaborated in Refs. [22, 23, 58], the existence of the pasta phases modifies the interaction between neutrinos and matter significantly. Our recent work [66] strongly suggests the possibility of dynamical formation of the pasta phases in collapsing cores from a crystalline lattice of spherical nuclei; effects of the pasta phases on the supernova explosions should be seriously discussed in the near future.

In the present article, we provide an overview of the physics and astrophysical background of the pasta phases for researchers in other fields, especially in soft condensed matter physics. We try to show that the pasta phases can be an interesting system for many researchers in various fields, not only for nuclear astrophysicists. The plan of this paper is as follows. In the remaining part of the present section, we first give a brief explanation of collapse-driven supernovae, neutron stars and materials in these objects. We then describe the basic physics and astrophysical consequences of the pasta phases. In Section 2, we discuss the similarity between the pasta phases and soft condensed matter. We then explain a theoretical framework used in our studies in Section 3, and show the results in Section 4. In this article, we generally set the Boltzmann constant $k_{\text{B}} = 1$.

1.1 Collapse-Driven Supernovae

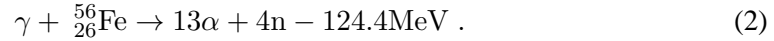
Stars evolve by burning light elements into heavier ones (see, e.g., Ref. [72]); here burning means nuclear fusion. The ultimate fate of the star is basically determined by its mass in the main sequence period, when the star is supported by thermal pressure of burning hydrogen nuclei (protons). Nuclear reactions of heavier nuclei require higher temperatures because of their greater Coulomb barrier. In the core of massive stars with $M \gtrsim 8M_{\odot}$, the temperature reaches a threshold to produce iron. Elements heavier than iron cannot be produced by nuclear fusion since the binding energy per nucleon of iron is the greatest among all the elements. Therefore iron nuclei, the major final product of a chain of the thermally driven nuclear reactions, accumulate in the core of massive stars at the end of their evolution.

As the nuclear burning proceeds and the mass of the iron core increases, two processes which tend to make the core unstable to collapse occur — electron capture, and photodisassociation of heavy nuclei. In the iron core the density is so high ($\sim 4 \times 10^9 \text{g cm}^{-3}$) that the

core is supported mainly by electron degeneracy pressure; degenerate electrons have extremely large momenta even at zero temperature due to the Pauli exclusion principle. When the electron Fermi energy exceeds 3.7 MeV, electron capture on iron nuclei occurs:



Since this reaction decreases the electron density, the electron degeneracy pressure decreases and can no longer support the iron core. This instability leads to contraction of the core. The other instability is triggered by photodissociation of iron nuclei, which occurs when the temperature of the core is $\gtrsim 5 \times 10^9$ K:



This is an endothermic reaction; thus it decreases the gas pressure and accelerates the collapse.

As the collapse of the core proceeds and the central density approaches the nuclear saturation density (normal nuclear density), $\rho_0 = 0.165$ nucleons $\text{fm}^{-3} \simeq 3 \times 10^{14}$ g cm^{-3} , the equation of state suddenly becomes hard because of a strong short-range repulsion between nucleons. Due to this hardening, the pressure becomes sufficiently high to halt the collapse, causing the inner region of the core to bounce. The outer region of the core continues to fall towards the center at supersonic velocities. Consequently, the bouncing inner core drives a shock wave into the infalling outer core. The initial energy of the shock is $\sim 10^{51}$ erg and is enough to blow off the stellar envelope, which results in an explosion of the star. However, the shock wave propagating through the outer core is weakened by several processes (see, e.g., Ref. [60]) which decrease the pressure and dissipate the energy behind the shock front. Consequently, the shock wave stalls in the outer core. Neutrinos emitted from the inner core will heat the matter behind the shock front (a process referred to as neutrino heating). If the neutrino heating is efficient enough, the stalled shock can be revived, reach the surface of the outer core, propagate beyond the core, and finally blow off the outer layer of the star; thereby producing a supernova explosion. The contracted core remains as a nascent neutron star.

The difference in the gravitational energy between the iron core and a neutron star is given by

$$\Delta E \simeq - \left(\frac{GM_{\text{core}}^2}{R_{\text{Fe core}}} - \frac{GM_{\text{core}}^2}{R_{\text{NS}}} \right) \simeq \frac{GM_{\text{core}}^2}{R_{\text{NS}}} \sim O(10^{53}) \text{ erg} , \quad (3)$$

where G is the gravitational constant, $M_{\text{core}} \sim 1M_{\odot}$ is the mass of the core, $R_{\text{Fe core}} \sim O(10^3)$ km is the initial radius of the iron core and the neutron star radius R_{NS} is about 10 km. Only one percent of this energy is injected into the gas blown off and 99 % is carried away by neutrinos ¹. In the supernova explosion, neutrinos interact with matter and will inject kinetic energy into it. Therefore detailed investigations of interactions between neutrinos and matter in supernova cores are necessary to understand the explosion mechanism (see, e.g., Refs. [6, 9, 18, 25, 36]).

¹The gravitational energy is emitted in all six flavors of neutrinos and anti-neutrinos almost equally. However, muon and tauon neutrinos (and anti-neutrinos) are not important for supernova explosions because they interact with matter extremely weakly. Thus, hereafter, the term ‘‘neutrino’’ denotes an electron neutrino.

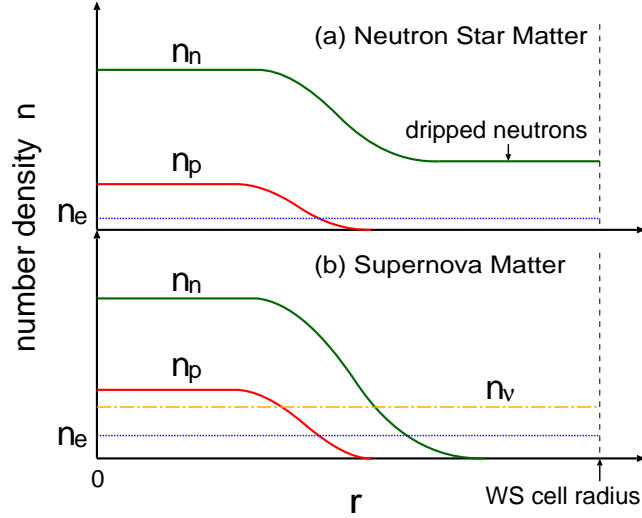


Figure 1: (Color) Schematic diagram of a Wigner-Seitz cell of neutron star matter (NSM) and supernova matter (SNM) where n_n , n_p , n_e and n_ν are the number densities of neutrons, protons, electrons and neutrinos respectively.

As the density in the core increases during the collapse, the mean free path of neutrinos l_ν decreases mainly due to the neutrino coherent scattering from nuclei via the weak neutral current. The amplitude of the coherent scattering is proportional to A , where A is the mass number of the nucleus. Therefore its cross section σ is proportional to A^2 [17], while that of the incoherent scattering is simply proportional to A . When the neutrino wavelength is much longer than the radius of the nucleus, the neutrino is coherently scattered by nucleons in the nucleus. In the collapsing iron core, a typical value of the wavelength λ_ν of a neutrino with energy E_ν is

$$\lambda_\nu = \frac{hc}{E_\nu} \simeq 2\pi \times 20 \text{ fm} \left(\frac{10 \text{ MeV}}{E_\nu} \right), \quad (4)$$

and that of the nuclear radius r_N is

$$r_N \simeq 1.2A^{1/3} \text{ fm} \simeq 5 \text{ fm} \left(\frac{A}{56} \right)^{1/3}. \quad (5)$$

The neutrino diffusion time scale is estimated by the random-walk relation:

$$\tau_{\text{diff}} \sim \frac{R^2}{cl_\nu}, \quad (6)$$

where R is the radius of the collapsing core and c is the speed of light. The dynamical time scale of the core collapse is comparable to the free-fall time scale:

$$\tau_{\text{dyn}} \sim \frac{1}{\sqrt{G\rho_{\text{core}}}}, \quad (7)$$

where ρ_{core} is the density of the core. When τ_{diff} is greater than τ_{dyn} (the corresponding density region is above $10^{11-12} \text{g cm}^{-3}$), neutrinos cannot escape from the inner core [55]; this phenomenon is called neutrino trapping. While neutrinos produced by electron capture remain in the inner core for the order of 10 msec, the lepton fraction Y_L , the lepton number per nucleon [$Y_L \equiv (n_e + n_\nu)/(n_n + n_p)$ where n_e , n_ν , n_n and n_p are the number densities of electrons, neutrinos, neutrons and protons], stays in a range of about 0.3 - 0.4. Trapped neutrinos build up a degenerate sea, which suppresses electron capture. Because the time scale of weak interaction processes is much shorter than $\tau_{\text{dyn}} \sim \tau_{\text{diff}}$, matter in the inner core is in β equilibrium with trapped neutrinos. At densities $\rho \lesssim \rho_0$, matter consists of nuclei, electrons (to maintain charge neutrality) and neutrinos, and we shall refer to this simply as supernova matter (SNM) [8, 30]. We show particle number density profiles in supernova matter in Fig. 1-(b). Since degenerate electrons are relativistic, screening effects are negligible and the electrons are uniformly distributed [38, 50, 63]. There also exist the uniform neutrino gas and neutron-rich nuclei: clusters of protons and neutrons. In a certain density region below the normal nuclear density, supernova matter could consist of nuclei with exotic shapes such as rod-like and slab-like nuclei rather than spherical ones, which are referred to as nuclear “pasta” (a further explanation will be given in Section 1.3). The pasta nuclei affect neutrino opacity of the supernova matter (see Section 1.4).

1.2 Neutron Stars

Let us see further evolution of the bounced core. After bounce, the core settles into hydrostatic equilibrium on its dynamical time scale and a protoneutron star is formed unless the core is not so heavy that it collapses to a black hole. The initial radius and temperature of the protoneutron star are ~ 100 km and ~ 10 MeV, respectively. Just after the bounce of the core, the proton fraction $x \equiv n_p/(n_n + n_p)$, and the lepton fraction of matter in the core are relatively high (both are around 0.3). As neutrinos escape from the protoneutron star, it cools down and electron capture, which is blocked by the degenerate neutrinos, proceeds (see, e.g., Ref. [74] for a recent review of cooling of neutron stars). Consequently matter gets neutron rich; the proton fraction $x \lesssim 0.1$ at around the normal nuclear density ρ_0 . At the same time, the radius of the object shrinks to ~ 10 km; a neutron star is formed.

Neutron stars are dense and compact objects supported by neutron degeneracy pressure and nuclear forces. The mass and the radius of a typical neutron star are $\simeq 1.4M_\odot$ and $\simeq 10$ km, respectively. The properties of dense matter and its equation of state are relatively well understood in the density region below $\sim \rho_0$. Thus the theoretical picture of neutron star structure is reasonably established in the lower density region (see, e.g., Ref. [33, 50] for reviews).

In Fig. 2 we show a schematic cross section of a typical cold neutron star below 10^9 K. The outermost part, the envelope, is a layer about several meters thick which consists of liquid ^{56}Fe (if there is accretion from its companion star, the envelope is covered by a layer of hydrogen and helium atoms). With increasing density (i.e., proceeding to the deeper region), weak interactions render nuclei neutron-rich via electron captures triggered by a large electron chemical potential. Matter becomes solid at a density $\rho \gtrsim 10^6 \text{g cm}^{-3}$, which consists of nuclei forming a bcc Coulomb lattice neutralized by a roughly uniform electrons. Then, at a density of about $\sim 4 \times 10^{11} \text{g cm}^{-3}$, nuclei become so neutron rich

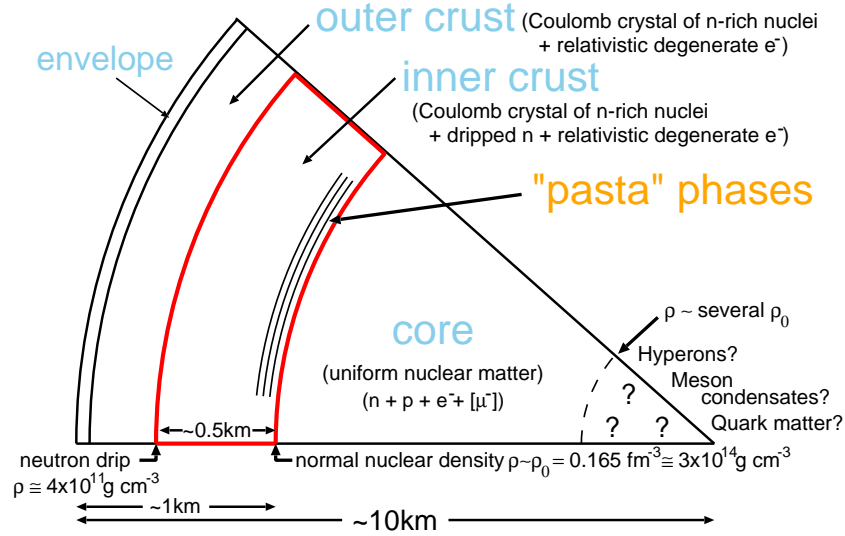


Figure 2: (Color) Schematic picture of the cross section of a neutron star.

that the last occupied neutron levels are no longer bound; neutrons begin to drip out of these nuclei. These “dripped” neutrons form a superfluid amid the neutron-rich nuclei. The crystalline region of the star is referred to as crust, which is divided into inner and outer crust; in the outer crust there are no neutrons outside nuclei, while in the inner crust there are. The inner crust extends from the neutron drip point to the boundary with the core at a density $\rho \lesssim \rho_0 \simeq 3 \times 10^{14} \text{ g cm}^{-3}$, where nuclei disappear and the system becomes uniform nuclear matter. Matter in these regions is called neutron star matter (NSM) [5, 7, 40]. A schematic picture of neutron star matter at subnuclear densities is shown in Fig. 1-(a). There exist dripped neutrons outside the neutron-rich nuclei. Degenerate electrons are uniformly distributed for the same reason as in the case of supernova matter. Another difference between supernova matter and neutron star matter is the lack of trapped degenerate neutrinos. This makes neutron star matter more neutron-rich than supernova matter in β equilibrium. In the deepest region of the inner crust corresponding to subnuclear densities (i.e., $\rho \lesssim \rho_0$), pasta nuclei could appear (see Section 1.3 for a further explanation). Although crusts of neutron stars are relatively thin ($\sim 1 \text{ km}$), they influence many observed phenomena [33, 50]. Effects of the pasta phases on these phenomena will be discussed in Section 1.4.

The physics of the density region above several times normal nuclear density is quite uncertain, and a variety of hadronic phases have been proposed, such as hyperonic matter, pion or kaon condensates, quark-hadron mixed phase and uniform quark matter, etc. (see, e.g., Ref. [21] and references therein for details). These are beyond the scope of the present article.

1.3 What is Nuclear “Pasta”?

In ordinary matter, atomic nuclei are roughly spherical. This may be understood in the liquid drop picture of the nucleus as being a result of the forces due to the surface tension

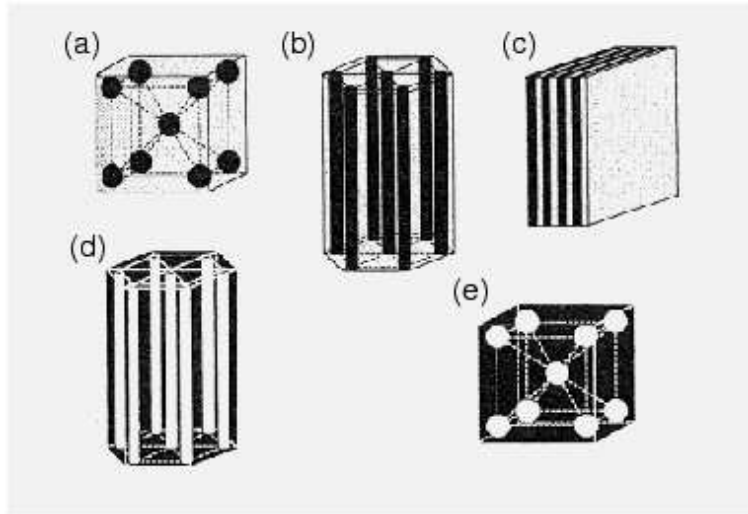


Figure 3: Nuclear “pasta.” The darker regions show the liquid phase, in which protons and neutrons coexist (i.e., the nuclear matter region); the lighter ones the gas phase, which is almost free of protons. Sequence (a)-(e) shows that of nuclear shape changes with increasing density. This figure is taken from Ref. [45].

of nuclear matter, which favors a spherical nucleus, being greater than those due to the electrical repulsion between protons, which tends to make the nucleus deform. When the density of matter approaches that of atomic nuclei, i.e., the normal nuclear density ρ_0 , nuclei are closely packed and the effect of the electrostatic energy becomes comparable to that of the surface energy. Consequently, at subnuclear densities around $\rho \lesssim \rho_0/2$, the energetically favorable configuration is expected to have remarkable structures as shown in Fig. 3; the nuclear matter region (i.e., the liquid phase of mixture of protons and neutrons) is divided into periodically arranged parts of roughly spherical (a), rod-like (b) or slab-like (c) shape, embedded in the gas phase and in a roughly uniform electron gas. Besides, there can be phases in which nuclei are turned inside out, with cylindrical (d) or spherical (e) bubbles of the gas phase in the liquid phase. As mentioned in the previous section, these transformations are expected to occur in the deepest region of neutron star inner crusts and in the inner cores of collapsing stars just before the star rebounds. Since slabs and rods look like “lasagna” and “spaghetti”, the phases with non-spherical nuclei are often referred to as “pasta” phases and such non-spherical nuclei as nuclear “pasta.” Likewise, spherical nuclei and spherical bubbles are called “meatballs” and “Swiss cheese”, respectively.

More than twenty years ago, Ravenhall *et al.* [53] and Hashimoto *et al.* [20] independently pointed out that nuclei with such exotic shapes² can be the most energetically stable due to the subtle competition between the nuclear surface and Coulomb energies as mentioned above. Let us here show this statement by a simple calculation using an incompressible liquid-drop model (see also Ref. [46]).

We consider five phases depicted in Fig. 3, which consist of spherical nuclei, cylindrical

²The “Swiss cheese” phase was considered earlier in Ref. [5] than the other pasta phases.

nuclei, planar nuclei, cylindrical bubbles and spherical bubbles, respectively. Each phase is taken to be composed of a single species of nucleus or bubble at a given nucleon density ρ averaged over the space. The total electrostatic energy including the lattice energy, which is the contribution to the Coulomb energy coming from neighbouring nuclei, is estimated by the Wigner-Seitz approximation.

In the present discussion, we assume that the nuclear matter region is incompressible and the nucleon density there is fixed at the normal nuclear density $\rho_0 = 0.165 \text{ fm}^{-3}$. We further assume that the proton fraction x_N in the nuclear matter region is fixed at $x_N = 0.3$ and that the dripped neutrons can be ignored for simplicity. These assumptions correspond to the situation of supernova matter [see Fig. 1-(b)]. Using a liquid-drop model, the total energy density of matter E_{tot} averaged over a single cell can be written as

$$E_{\text{tot}} = \begin{cases} uw_{\text{bulk}} + w_{\text{surf}} + w_{\text{C+L}} + E_e & \text{(nuclei) ,} \\ (1-u)w_{\text{bulk}} + w_{\text{surf}} + w_{\text{C+L}} + E_e & \text{(bubbles) ,} \end{cases} \quad (8)$$

where u is the volume fraction of the nuclei or bubbles, w_{bulk} is the bulk energy density of the nuclear matter region, w_{surf} , $w_{\text{C+L}}$, and E_e are the nuclear surface, total electrostatic, and electron energy densities, respectively. Under the assumption of neglecting the dripped neutrons, the volume fraction u of nuclei [bubbles] is given as $u = \rho/\rho_0$ [$u = 1 - (\rho/\rho_0)$]. The electron number density n_e , which is assumed to be uniform here, is $n_e = \rho_0 x_N u$ [$n_e = \rho_0 x_N (1 - u)$]. As we consider incompressible nuclear matter with fixed proton fraction x_N , in the expression of E_{tot} [Eq. (8)] only w_{surf} and $w_{\text{C+L}}$ depend on the nuclear shape at a given ρ . Thus the energetically most stable nuclear shape can be determined by comparing $w_{\text{surf}} + w_{\text{C+L}}$ between each nuclear shape.

The surface energy per unit volume w_{surf} is expressed as

$$w_{\text{surf}} = \frac{\sigma u d}{r_N}, \quad (9)$$

where σ is the surface tension, r_N is the radius (or the half width) of nuclei or bubbles and d is the dimensionality of the nuclear shape defined as $d = 1$ for slabs, $d = 2$ for cylinders or cylindrical holes and, $d = 3$ for spheres or spherical holes. We assume σ to be constant and set $\sigma = 0.73 \text{ MeV fm}^{-2}$ [52].

In the Wigner-Seitz approximation, one replaces the actual unit cell by a spherical one for $d = 3$, a cylindrical one for $d = 2$, and a planar one for $d = 1$, which are electrically neutral and have an equal volume to the actual cell. Using this approximation, the total electrostatic energy per unit volume $w_{\text{C+L}}$ yields

$$w_{\text{C+L}} = 2\pi(e x_N \rho_0 r_N)^2 u f_d(u), \quad (10)$$

with

$$f_d(u) = \frac{1}{d+2} \left[\frac{2}{d-2} \left(1 - \frac{du^{1-2/d}}{2} \right) + u \right]. \quad (11)$$

Minimizing $w_{\text{surf}} + w_{\text{C+L}}$ with respect to r_N leads to a simple condition for all the five nuclear shapes considered here:

$$w_{\text{surf}} = 2w_{\text{C+L}}. \quad (12)$$

Thus $w_{\text{surf}} + w_{\text{C+L}}$ is given as

$$w_{\text{surf}} + w_{\text{C+L}} = \rho_0 \zeta_s g_d(u), \quad (13)$$

with $\zeta_s \equiv 3 \left(\frac{9}{5} \pi x_N^2 e^2 \sigma^2 \frac{1}{\rho_0} \right)^{1/3}$ and $g_d(u) \equiv u \left(\frac{5}{18} d^2 f_d(u) \right)^{1/3}$.

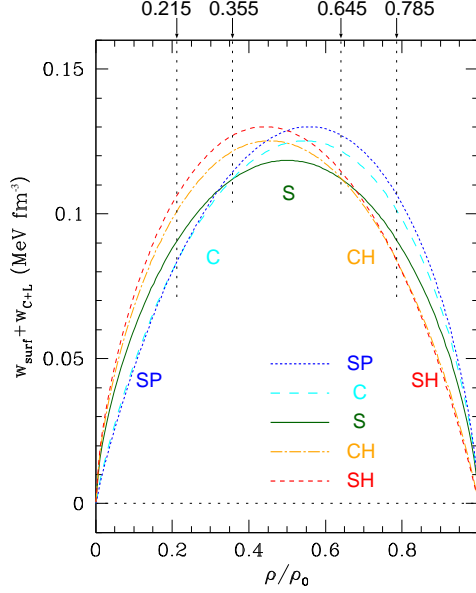


Figure 4: (Color) $w_{\text{surf}} + w_{\text{C+L}}$ given by Eq. (13) as a function of the nucleon number density ρ . The symbols SP, C, S, CH, and SH stand for nuclear shapes, i.e., sphere, cylinder, slab, cylindrical hole, and spherical hole, respectively. The transition points locate symmetrically with respect to the point of $\rho = \rho_0/2$ in the case of neglecting the bulk contribution.

We have plotted in Fig. 4 the summation of the nuclear surface and total electrostatic energy densities, $w_{\text{surf}} + w_{\text{C+L}}$, given by Eq. (13) for each five nuclear shape. At densities below ρ_0 , the system must have an inhomogeneous structure of some kind because matter is assumed to be incompressible here. The point at $\rho = \rho_0$, where the lines for all shapes and the line of $w_{\text{surf}} + w_{\text{C+L}} = 0$ cross each other, corresponds to uniform nuclear matter. It can be seen from Fig. 4 that the phase with spherical nuclei gives the lowest value of $w_{\text{surf}} + w_{\text{C+L}}$ at lower densities below $0.215 \rho_0$, and, with increasing density, the most stable shape of the nuclear matter region changes as

$$\text{sphere} \rightarrow \text{cylinder} \rightarrow \text{slab} \rightarrow \text{cylindrical hole} \rightarrow \text{spherical hole} \rightarrow \text{uniform} . \quad (14)$$

Even though the pasta phases were favored energetically, whether or not they are actually present in the star depends on occurrence of the dynamical processes leading to their formation. Our recent dynamical simulations [66, 67, 68, 69] have almost solved this problem (see Section 4).

1.4 Astrophysical Consequences

The presence of nuclear pasta would affect some astrophysical phenomena. It is noted that the pasta phases can occupy half of the total mass of the neutron star crusts [34] and 10 – 20% of the mass of supernova cores in the later stage of the collapse [58]. In this section we explain effects of the pasta phases on the neutrino trapping and the core dynamics of supernovae, pulsar glitches and cooling of neutron stars.

1.4.1 Supernova Explosions

Formation of the pasta phases in collapsing cores would influence neutrino transport in the cores. As mentioned in Section 1.1, this is considered to be crucial for reproduction of supernova explosions by simulation studies. Due to neutrino-nucleus coherent scattering, the pasta phases have a large effect on the neutrino opacity of supernova matter [65, 67, 68]. If one takes account of the pasta phases, they replace uniform matter close to a boundary between uniform and non-uniform phases; the neutrino opacity of the pasta phases is significantly larger than that of uniform nuclear matter. This enhancement is elaborated with quantum molecular dynamic (QMD) simulations in Refs. [22, 23, 58] (see also Section 3 for the framework of the QMD). The cross section for coherent neutrino scattering is approximated to be proportional to the static structure factor $S_{\text{nn}}(q)$ of neutrons, where q is the wave number of the momentum transfer. The static structure factor is obtained by the Fourier transform of a radial distribution function which represents two-point correlations. This quantity is remarkably increased near the wave number corresponding to the reciprocal lattice vector; in the case of uniform matter this peak cannot be seen. We show in Fig. 5 the static structure factor $S_{\text{nn}}(q)$ calculated for nucleon distributions of $T = 1, 2$ and 3 MeV at $x = 0.3$ and $\rho = 0.175 \rho_0$, where the phase with rod-like nuclei appears at low temperatures. The nucleon distributions are obtained by our QMD simulations, which will be explained in Section 4. A peak around $q = 0.25 - 0.3 \text{ fm}^{-1}$ at each temperature indicates enhancement of the neutrino opacity; at 1 MeV the cross section around the peak exceeds one hundred times that for uniform matter. With increasing temperature, the peak height drops because nuclei start to melt (see phase diagrams in Section 4).

The existence of pasta nuclei also affects the hydrodynamics of supernova cores. Phase transition from a bcc lattice to uniform nuclear matter is considerably smoothed by the presence of the pasta phases, which modifies the equation of state used in core collapse simulations [53]. In addition to the equation of state, the pasta phases also have an effect on the other hydrodynamic properties of supernova matter due to their different elastic properties from those of a crystalline lattice of spherical nuclei or uniform nuclear matter. Although the above effects are crucial for supernova explosions, it is not obvious how they affect the explosions in detail; this should be investigated by simulation studies of supernovae in the future.

1.4.2 Pulsar Glitches

Pulsars are neutron stars emitting periodic pulses, with a period equal to that of the rotation of the star. In more than 20 pulsars, sudden decreases of pulse periods, i.e., spinups of neutron star crusts, are observed. These phenomena are called “glitches.” There is not yet

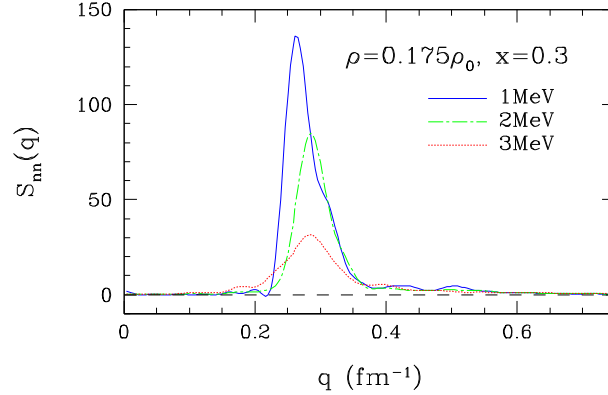


Figure 5: (Color) Static structure factor of neutrons $S_{nn}(q)$ calculated for nucleon distributions at $x = 0.3$, $\rho = 0.175 \rho_0$ (rod phase at low temperatures), and at temperatures of 1MeV (solid line), 2MeV (dash-dotted line) and 3MeV (dotted line).

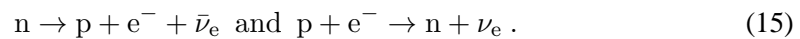
a consensus about the mechanism of glitches but a widely accepted theory is the vortex pinning model [4].

In neutron star crusts, dripped neutrons form a superfluid and neutron-rich nuclei, which may be regarded as a normal fluid, act as a pinning center for vortex lines in the neutron superfluid. In the vortex pinning model glitches represent vorticity jumps following catastrophic unpinning of the vortex lines. Since migrations of vortex lines result in transport of angular momentum, this leads to spinups of the crusts. It is obvious that the existence of the nuclear pasta would have a large influence on pinning. However, the force needed to pin the vortices and the pinning rate have yet to be clarified completely even for a bcc lattice of spherical nuclei, rather than for non-spherical nuclei [26].

There is another representative model of pulsar glitches: the starquake model [54]. According to this model, a sudden starquake of the neutron star crust decreases the moment of inertia and hence increases the angular velocity. Nuclei in the crust form a solid, Coulomb lattice. The rigidity of the solid crust restores the force against deformation. When the stress in the crust reaches a critical value, the crust cracks. The existence of the pasta phases instead of the normal bcc lattice reduces the maximum elastic energy that can be stored in the crust because, as will be discussed in Section 2, the pasta phases have directions in which restoring force does not act like liquid crystals [49]. Thus the pasta phases would reduce the strength of each glitch and shorten the time separation between glitches in this scenario.

1.4.3 Cooling of Neutron Stars

In the early epoch of the neutron star cooling, the main process of energy loss by neutrinos is the so-called URCA process:

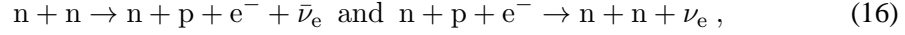


These reactions are dominant in the case that matter in the neutron star is hot and non-degenerate. However, when the matter becomes cold and degenerate as in a neutron star,

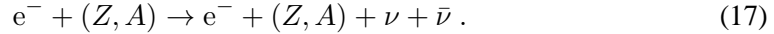
the URCA process is strongly suppressed by the energy and momentum conservation laws.

The presence of non-spherical nuclei would accelerate the cooling of neutron stars by opening the direct URCA reactions which are unlikely to occur for spherical nuclei [34]. This stems from the fact that, in non-spherical nuclei, protons have a continuous spectrum at the Fermi surface in the elongated directions.

The following reactions are generally accepted as the mechanism of generating neutrinos in cold and degenerate neutron stars:



which is referred to as the modified URCA process, and neutrino pair bremsstrahlung by electrons in the crust:



In the modified URCA process, a bystander neutron absorbs the momentum and relaxes kinematical constraints.

Pasta nuclei suppress the bremsstrahlung rate [27, 51]. If we assume that neutrino bremsstrahlung is dominated by the lowest reciprocal lattice vectors for which form factors do not vanish, the number of these vectors for each dimensional lattice leads to the neutrino emission rate of spherical, cylindrical and planar nuclei in the ratio of 6:3:1. If the nucleons in the core undergo a transition to a superfluid and/or superconducting state, the modified URCA process is suppressed by a factor of $\sim e^{-\Delta/k_B T}$, where Δ is the superfluid energy gap. In this case bremsstrahlung is dominant and the neutrino emission is suppressed efficiently as a consequence of the presence of pasta phases.

2 Pasta Phases as Soft Condensed Matter

Nuclear systems can be regarded as complex fluids of nucleons. Complex fluids are the systems in which scales of the fluid and their constituents cannot be separated clearly; both scales are strongly connected with each other. Such characteristic can be seen in various soft condensed matter systems. For example, polymer systems are one of the typical complex fluids (description of polymer systems in the present section is mainly based on an instructive review [28]). Actually, similar spatial structures to nuclear pasta as shown in Fig. 3 can be seen in some polymer systems such as domain structures in solutions and melts of block copolymers. Thus it would be interesting to compare the hierarchical structure of nuclear systems with that of polymer systems.

Polymers are made up of monomers connected by covalent bondings and their degrees of polymerization are quite large (> 100). Consequently, in polymer systems, the scale of constituents is as large as that of macroscopic phenomena such as phase separation of the domain structures. Thus polymer systems behave as complex fluids. In nuclear systems, the nature of a complex fluid is caused by strong and short range nuclear force.

In Fig. 6, we show the hierarchical structures of nuclear systems and of polymer systems. Nuclear pasta phases and domain structures of block copolymers can be classified in the semimacroscopic scale. Thus theoretical methods based on the mesoscopic or semi-macroscopic scales are practical for studying these systems. In the study of polymer systems, the density functional theory and the Ginzburg-Landau theory correspond to such

Spatial scale	Nuclear system			Polymer system			
	Hierarchy	Characteristic length (fm)	Characteristic ratio	Hierarchy	Characteristic length (m)	Characteristic ratio	
microscopic	nucleon	1	1	atom monomer	10^{-10} - 10^{-9}	1	
semimicroscopic	cluster molecular structure	1 - several	1 - several	internucleon int. pairing correlation	segment	10^{-9} - 10^{-8}	1 - 10
				interatomic int.			
mesoscopic	nucleus	several - 10	several - 10	mean-field pot.	configuration of polymer	10^{-9} - 10^{-4}	1 - 10^5
				surface tension Coulomb int.			
semimacroscopic	nuclear pasta	10 - 100	10 - 100	equation of state	domain structure	10^{-6} - 10^{-3}	10^3 - 10^6
				constitutive equation	viscoelastic substance	$> 10^{-10}$	$> 10^6$
macroscopic	nuclear matter	> 100	> 100				

Figure 6: Hierarchical structures of nuclear system and of polymer system. We refer to Ref. [28] for polymer system.

approaches. In nuclear physics, we have the Thomas-Fermi theory and the liquid-drop model, which are based on the scale of the nucleon density profile and of the nucleus, respectively. Actually, thermodynamic properties of the pasta phases and phase diagrams at zero-temperature have been investigated so far mainly by these approaches.

However, the nature of complex fluids of nuclear systems sets limits on the validity of the above methods. They cannot be used for investigating phenomena in which microscopic degrees of freedom are important: formation process of the pasta phases, thermal fluctuations and melting of the pasta structures are typical examples. However, due to the short range nuclear interaction, characteristic ratio of the macroscopic or semimacroscopic scale in nuclear systems is much smaller than that of polymer systems (see Fig. 6). Such a small characteristic ratio enables us to study the pasta phases by microscopic approaches based on the nucleonic degrees of freedom. Our simulations are performed using one of these methods, which will be explained in the next section.

Similarity between the pasta phases and some phases of liquid crystals should be also mentioned here. For the pasta phases with rod-like nuclei and slab-like nuclei, there are directions in which the system is translationally invariant. Consequently, any restoring forces do not act along such directions. As noted by Pethick and his coworkers [49, 50], this situation is analogous with a liquid crystal rather than with a rigid solid. Elastic properties of the phases with rod-like nuclei and with slab-like ones are thus characterized by elastic constants used for the corresponding liquid crystal phases, i.e., columnar phases and smectics A, respectively.

For the layered phases such as smectic A liquid crystals and the pasta phase with slab-like nuclei, the energy density E_{el} due to displacement ϵ of layers in their normal direction (taken to be parallel to the z -axis) can be written as [13]

$$E_{\text{el}} \simeq \frac{B}{2} \left(\frac{\partial \epsilon}{\partial z} \right)^2 + \frac{K_1}{2} (\nabla_{\perp}^2 \epsilon)^2 + O(\epsilon^3), \quad (18)$$

where ∇_{\perp} shows the derivative on the x - y plane. The elastic constants B and K_1 are associated with change of the layer spacing and with bending of the slabs.

For the two-dimensional triangular lattice in the columnar phase of liquid crystals or in the pasta phase with rod-like nuclei, the energy density due to a two-dimensional displacement vector $\epsilon = (\epsilon_x, \epsilon_y)$ of rods running along the z -axis is given by [13]

$$E_{\text{el}} \simeq \frac{B}{2} (\nabla_{\perp} \cdot \epsilon)^2 + \frac{C}{2} \left[\left(\frac{\partial \epsilon_x}{\partial x} - \frac{\partial \epsilon_y}{\partial y} \right)^2 + \left(\frac{\partial \epsilon_x}{\partial y} + \frac{\partial \epsilon_y}{\partial x} \right)^2 \right] + \frac{K_3}{2} \left(\frac{\partial^2 \epsilon}{\partial z^2} \right)^2 + O(\epsilon^3). \quad (19)$$

The elastic constant B is associated with uniform translational compression or dilation, C with transverse shear and K_3 with bending of the rods.

Now let us discuss thermodynamic stability of the phase with slab-like nuclei. According to the Landau-Peierls argument, strict long range positional order of layered phases will be destroyed at finite temperatures [31]. Physically, the elastic constant B for compression of the spacing between slab-like nuclei should be comparable to the Coulomb energy density:

$$B \sim w_{\text{C+L}}, \quad (20)$$

and the elastic constant for bending of slab-like nuclei K_1 should have dependence of the surface energy density times squared of the internuclear spacing l :

$$K_1 \sim w_{\text{surf}} l^2 \sim w_{\text{C+L}} l^2, \quad (21)$$

here we use the fact that w_{surf} and $w_{\text{C+L}}$ are comparable in the equilibrium state [Eq. (12)]. The above expressions are consistent with results of an explicit calculation in Ref. [49].

For the one-dimensional layered lattice, the mean-square displacement can then be evaluated within the harmonic approximation as [11]

$$\langle \epsilon^2 \rangle \sim \frac{T}{\sqrt{BK_1}} \ln \left(\frac{L}{l} \right) \sim \frac{T}{w_{\text{C+L}} l} \ln \left(\frac{L}{l} \right), \quad (22)$$

where L is the one-dimensional length scale of the extension of the slab. The Landau-Peierls instability for an infinite one-dimensional layered lattice can be seen by the logarithmic divergence of $\langle \epsilon^2 \rangle$ for large L .

Typical value of the interlayer spacing is $l \simeq 20$ fm. As can be seen from Fig. 4, $w_{\text{C+L}}$ in the supernova matter is $\sim 10^{-1}$ MeV fm $^{-3}$. Employing the Lindemann criterion $\langle \epsilon^2 \rangle / l^2 \sim 0.1$ for melting of the lattice, limits of the extension L are given by Eq. (22) as $\ln(L/l) \lesssim 100$ at $T \simeq 1$ MeV and $\ln(L/l) \lesssim 10$ at $T \simeq 10$ MeV. In the initial phase of the stellar collapse before the bounce of the core, the temperature of the supernova matter is the order of 1 MeV and the limit of L is even much larger than the radius of the core. Thus the Landau-Peierls instability does not matter in this stage.

In the neutron star inner crusts, temperature is ~ 0.1 MeV. The proton fraction in nuclei x_{N} is about one-third smaller than that for supernova matter; as can be seen from Eq. (10), $w_{\text{C+L}}$ in neutron star matter is thus $w_{\text{C+L}} \sim 10^{-2}$ MeV fm $^{-3}$ [other relevant quantities are comparable in the both cases]. Following the same way as in the above case, the limit of L is given by $\ln(L/l) \lesssim 100$, which is even much larger than the radius of neutron stars. The

phase with slab-like nuclei in neutron star crusts is thus stable in reality with respect to the Landau-Peierls instability.

Let us then estimate the temperature at which the lattice of the rod-like nuclei melts. For the two-dimensional triangular lattice, the mean-square displacement is [11]

$$\langle \epsilon^2 \rangle \sim \frac{T}{(B + 2C)\sqrt{\lambda l}}, \quad (23)$$

where $\lambda \equiv \sqrt{2K_3/(B + 2C)}$. An explicit calculation in Ref. [49] shows that values of the elastic constants are $B \sim w_{C+L}$, $C \simeq w_{C+L}$ and $K_3 \simeq 0.05 w_{C+L} l^2$. Using the Lindemann criterion and the above typical values for l and w_{C+L} , one can estimate the melting temperature $T_m \gtrsim 10$ MeV for supernova matter and $T_m \gtrsim 1$ MeV for neutron star matter. In the above estimate, however, decrease of the surface tension due to the evaporation of nucleons and thermal broadening of the nuclear density profile is not taken into account. Thus the melting temperature for supernova matter would be smaller than the above value in the real situation. More elaborated calculations on the Landau-Peierls instability and of the melting temperature can be seen in Refs. [43, 64, 65].

In closing the present section, let us briefly mention several phases which are not shown in Fig. 3. In block copolymer melts, various phases with complicated structures, e.g., gyroid phase, perforated lamellar phase and double diamond phase, etc., have been observed. As will be seen in Section 4, our simulations suggest that phases with multiply connected structures also appear in the nuclear systems (see also Ref. [50]). This point should be examined in the future study³.

3 Molecular Dynamics for Nucleons

Since the seminal works by Ravenhall *et al.* [53] and Hashimoto *et al.* [20], properties of the pasta phases in equilibrium states have been investigated using various nuclear models. They include studies on phase diagrams at zero temperature [34, 45, 47, 59, 64, 65, 70] and at finite temperatures [32]. These earlier works have confirmed that, for various nuclear models, the nuclear shape changes in the way of Eq. (14) as predicted by Refs. [20, 53].

In these earlier works, however, a liquid drop model or the Thomas-Fermi approximation is used with an assumption on the nuclear shape (except for Ref. [70]). Thus the phase diagram at subnuclear densities and the existence of the pasta phases should be examined without assuming the nuclear shape. It is also noted that at temperatures of several MeV, which are relevant to the collapsing cores, effects of thermal fluctuations on the nucleon distribution are significant. However, these thermal fluctuations cannot be described properly by mean-field theories such as the Thomas-Fermi approximation used in the previous work [32].

In contrast to the equilibrium properties, dynamical or non-equilibrium aspects of the pasta phases had not been studied until recently except for some limited cases [24, 50]. Thus it had been unclear even whether or not the pasta phases can be formed dynamically within the time scale of the cooling of neutron stars nor whether or not the formation of

³In the nuclear pasta phases, the long range Coulomb interaction plays an essential role. Thus a Helfrich-type simple local theory for the nuclear surface cannot be applied to the present problem.

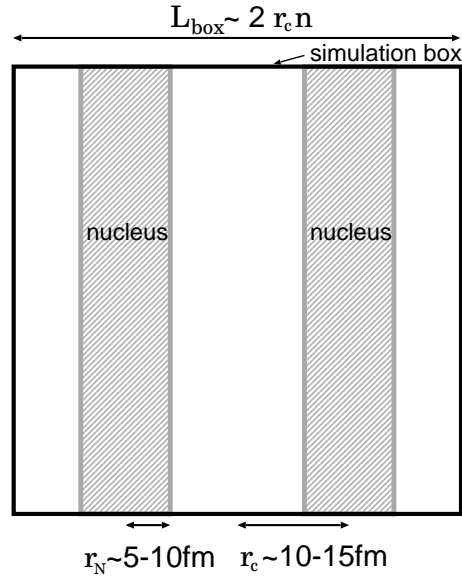


Figure 7: Typical length scales in the simulated system. The grey regions show “pasta” nuclei with the typical values of the half width $r_N \sim 5-10$ fm, and of the separation $r_c \sim 10-15$ fm. The typical value of the average nucleon density in the simulation box is about half of the normal nuclear density $\rho_0 = 0.165 \text{ fm}^{-3}$.

the pasta phases and the transitions between them can be realized under non-equilibrium conditions in collapsing stellar cores. Especially, the latter problem is highly non-trivial because these processes are accompanied by drastic changes of nuclear shape.

To solve the above problems, molecular dynamic approaches for nucleon many-body systems (a comprehensive overview is given by Ref. [16]) are suitable. They treat the motion of the nucleonic degrees of freedom and can describe thermal fluctuations and many-body correlations beyond the mean-field level. Molecular dynamics for nucleons were originally developed for studying nuclear reactions, especially the dynamics of heavy ion collisions. Nowadays there are various versions including the fermionic molecular dynamics (FMD) [14, 15], the antisymmetrized molecular dynamics (AMD) [44] and the quantum molecular dynamics (QMD) [1, 2], etc., which differ in the form of the trial wave functions. They are now widely used in studies on nuclear structure as well as nuclear reactions.

Among these models, QMD is the most practical for studying the pasta phases, which allows us to treat large systems consisting of several nuclei. The typical length scale r_c of half of the inter-structure is $r_c \sim 10$ fm and the density region of interest is around half of the normal nuclear density $\rho_0 = 0.165 \text{ fm}^{-3}$. The total nucleon number N necessary to reproduce n structures in the simulation box is $N \sim \rho_0 (2r_c n)^3$ (for slabs). It is thus desirable to use $\sim 10^4$ nucleons in order to reduce boundary effects. Such large systems are difficult to be handled by FMD and AMD, whose calculation costs increase as $\sim N^4$, but are tractable for QMD, whose calculation costs increase as $\sim N^2$ like ordinary classical molecular dynamics calculations (we will see the reason of this difference later).

It is also noted that we mainly focus on the nuclear structure from mesoscopic to macro-

scopic scales (see Section 2), where the exchange effect would be less important⁴. Therefore, it is expected that QMD is a reasonable approximation for studying the pasta phases even though it is less elaborate on the treatment of the exchange effect than FMD and AMD. Especially, at finite temperatures of several MeV, validity of QMD is ensured because the shell structure (see Refs. [10, 35, 48] for the shell effects in the pasta phases) caused from the exchange effect is washed out by thermal fluctuations above $T \sim 3$ MeV.

3.1 Framework of QMD

A general startpoint of constructing molecular dynamic approaches for nucleons is the time dependent variational principle:

$$0 = \delta \int_{t_1}^{t_2} dt \langle \Psi(t) | i\hbar \frac{d}{dt} - \hat{H} | \Psi(t) \rangle, \quad (24)$$

where the time integral in the right hand side is the action. If the variation δ of the state $\Psi(t)$ or $\Psi^*(t)$ is unrestricted in the whole Hilbert space except for the fixed end points at time t_1 and t_2 , Eq. (24) gives the usual time dependent Schrödinger equation. Let us now restrict the space to be considered by taking some trial many-body state $|\Phi\{Q(t)\}\rangle$, which contains a set of dynamical variables (complex in general) $Q(t) = \{q_1(t), q_2(t), \dots\}$.

In QMD, we assume each single-particle state ϕ_i of nucleon i is a Gaussian wave packet and take the centers of positions and momenta of the wave packets, $\mathbf{R}_i(t)$ and $\mathbf{P}_i(t)$, as a set of the dynamical variables $Q(t) = \{\mathbf{R}_i(t), \mathbf{P}_i(t); i = 1, \dots, N\}$;

$$\phi_i(\mathbf{r}) = \langle \mathbf{r} | \phi_i \rangle = \frac{1}{(2\pi\sigma^2)^{3/4}} \exp \left[-\frac{(\mathbf{r} - \mathbf{R}_i)^2}{4\sigma^2} + \frac{i}{\hbar} \mathbf{r} \cdot \mathbf{P}_i \right], \quad (25)$$

where σ is a parameter related to the extension of the wave packet in the coordinate space. Thus, σ is set $\sim O(1)$ fm for nucleons in nuclear matter at around the normal nuclear density. The total N -nucleon wave function $|\Phi\{Q(t)\}\rangle$ is constructed as a direct product of single-nucleon states defined by Eq. (25)⁵

$$|\Phi\rangle = |\phi_1\rangle \otimes |\phi_2\rangle \otimes \dots \otimes |\phi_N\rangle. \quad (26)$$

Employing the time-dependent variational principle with the above trial state $|\Phi\rangle$ yields the following equations of motion (QMD EOM):

$$\begin{aligned} \dot{\mathbf{R}}_i &= \frac{\partial \mathcal{H}}{\partial \mathbf{P}_i}, \\ \dot{\mathbf{P}}_i &= -\frac{\partial \mathcal{H}}{\partial \mathbf{R}_i}, \end{aligned} \quad (27)$$

⁴This can be seen by comparing the typical values of the exchange energy for these larger scales and of the energy difference between two successive phases with non-spherical nuclei. See, e.g., Ref. [68] for detail.

⁵In FMD and AMD, $|\Phi\{Q(t)\}\rangle$ is a Slater determinant of single-nucleon states instead of a direct product of them. Therefore, computational costs for calculating the expectation value of the Hamiltonian in FMD and AMD are larger than those in QMD by a factor of N^2 .

where $\mathcal{H}(\{Q(t)\})$ is the expectation value of the Hamiltonian \hat{H} :

$$\mathcal{H} \equiv \langle \Phi | \hat{H} | \Phi \rangle . \quad (28)$$

We note that the above semiclassical equations of motion, which incorporate the effect of the uncertainty principle, have the same form as the classical Hamilton's equations.

The trial wave function of QMD given by Eq. (26) does not possess antisymmetric properties. Thus it is necessary to incorporate effects of the Pauli exclusion principle in some way to reproduce fermionic nature: one of the solutions is introducing the Pauli potential V_{Pauli} . The Pauli potential, a two-body repulsive potential, which depends on the relative momentum as well as the relative coordinate distance, mimics the Pauli principle by reproducing the exchange repulsive force phenomenologically, i.e., by suppressing the phase space density of identical particles.

There are several forms of the Pauli potential; the following Gaussian form is one example:

$$V_{\text{Pauli}} = C_P \left(\frac{\hbar}{q_0 p_0} \right)^3 \exp \left[-\frac{(\mathbf{R}_i - \mathbf{R}_j)^2}{2q_0^2} - \frac{(\mathbf{P}_i - \mathbf{P}_j)^2}{2p_0^2} \right] , \quad (29)$$

where C_P , q_0 and p_0 are parameters. The parameters q_0 and p_0 determine the range of the phase space distance where the exchange repulsion acts. They are thus set so that their product equals to the volume element of the phase space: $q_0 \cdot p_0 \sim h$.

However, we have to mention that the genuine effect of the Pauli principle caused by antisymmetrization is a N -body correlation, not a two-body effect. Therefore, the Pauli potential which try to imitate the Pauli principle by two-body interaction cannot exactly describe quantum correlations and quantum statistical properties. Using this framework, we thus cannot obtain correct results for quantities sensitive to the quantum fluctuations in the many-body system, such as the specific heat at low temperatures [42].

3.2 Model Hamiltonian

In our studies on the pasta phases, we have used a QMD model Hamiltonian developed by Maruyama *et al.* [37]. This model Hamiltonian consists of four parts:

$$\mathcal{H} = K + V_{\text{Pauli}} + V_{\text{nucl}} + V_{\text{Coulomb}} , \quad (30)$$

where K is the kinetic energy; V_{Pauli} is the Pauli potential of the Gaussian form given by Eq. (29); V_{nucl} is the nuclear interaction which contains the Skyrme potential (an effective zero-range nuclear interaction), symmetry energy, and momentum dependent potential; V_{Coulomb} is the Coulomb energy between protons.

The parameters in the Pauli potential are determined by fitting the kinetic energy of the free Fermi gas at zero temperature. The above model Hamiltonian reproduces the properties of nuclear matter around the normal nuclear density (i.e., the saturation density, binding energy, symmetry energy, and incompressibility), and of finite nuclei in the ground state, especially of heavier ones relevant to our interest [29, 37]. Other properties of this Hamiltonian, which are important for the pasta phases (e.g., the surface tension) are investigated in Ref. [68]. It is also confirmed that a QMD Hamiltonian close to this model provides a good description of nuclear reactions including the low energy region (several MeV per nucleon) [41].

4 Simulations and Results

Using the framework of QMD, we have solved the following two major questions [66, 67, 68, 69]. 1) Whether or not the pasta phases are formed by cooling down hot uniform nuclear matter in a finite time scale smaller than that of the neutron star cooling? 2) Whether or not transitions between the pasta phases can occur by compression of matter during the collapse of a star? In the present section, we would like to review our these works.

In our simulations, we treated the system which consists of neutrons, protons, and electrons in a cubic box with periodic boundary condition. The system is not magnetically polarized, i.e., it contains equal numbers of protons (and neutrons) with spin up and spin down. Relativistic degenerate electrons which ensure charge neutrality can be regarded as a uniform background because electron screening is negligibly small at relevant densities around ρ_0 [38, 50, 63]. Consequently, one must take account of the long-range nature of the Coulomb interaction (see also a discussion in Ref. [62]). We calculate the Coulomb interaction by the Ewald summation procedure [3, 19] taking account of the Gaussian charge distribution of the proton wave packets (see Appendix A in Ref. [68]).

4.1 Realization of the Pasta Phases from Hot Uniform Matter

In Refs. [67, 68], we showed that the pasta phases are produced from hot uniform nuclear matter and we studied phase diagrams at zero temperature. In these works, we first prepared a uniform hot nucleon gas at a temperature $T \sim 20$ MeV as an initial condition equilibrated for $\sim 500 - 2000$ fm/ c in advance. To realize the ground state of matter, we then cooled it down slowly until the temperature got ~ 0.1 MeV or less for $O(10^3 - 10^4)$ fm/ c , keeping the nucleon number density constant. In the cooling process, we mainly used the frictional relaxation method (equivalent to the steepest descent method), which is given by the physically grounded QMD equations of motion [Eq. (27)] plus small friction terms:

$$\begin{aligned}\dot{\mathbf{R}}_i &= \frac{\partial \mathcal{H}}{\partial \mathbf{P}_i} - \xi_R \frac{\partial \mathcal{H}}{\partial \mathbf{R}_i}, \\ \dot{\mathbf{P}}_i &= -\frac{\partial \mathcal{H}}{\partial \mathbf{R}_i} - \xi_P \frac{\partial \mathcal{H}}{\partial \mathbf{P}_i}.\end{aligned}\tag{31}$$

Here the friction coefficients ξ_R and ξ_P are positive definite, which determine the relaxation time scale.

The resulting typical nucleon distributions of cold matter at subnuclear densities are shown in Figs. 8 and 9 for proton fraction of matter $x = 0.5$ and 0.3 , respectively. We see from these figures that the phases with rod-like and slab-like nuclei, cylindrical and spherical bubbles, in addition to the phase with spherical nuclei are reproduced. The above simulations show that the pasta phases can be formed dynamically from hot uniform matter within a time scale $\tau \sim O(10^3 - 10^4)$ fm/ c .

4.2 Equilibrium Phase Diagrams

As has been mentioned in Section 3, QMD provides a good description of thermal fluctuations and is suitable for investigating the pasta phases at finite temperatures. We show

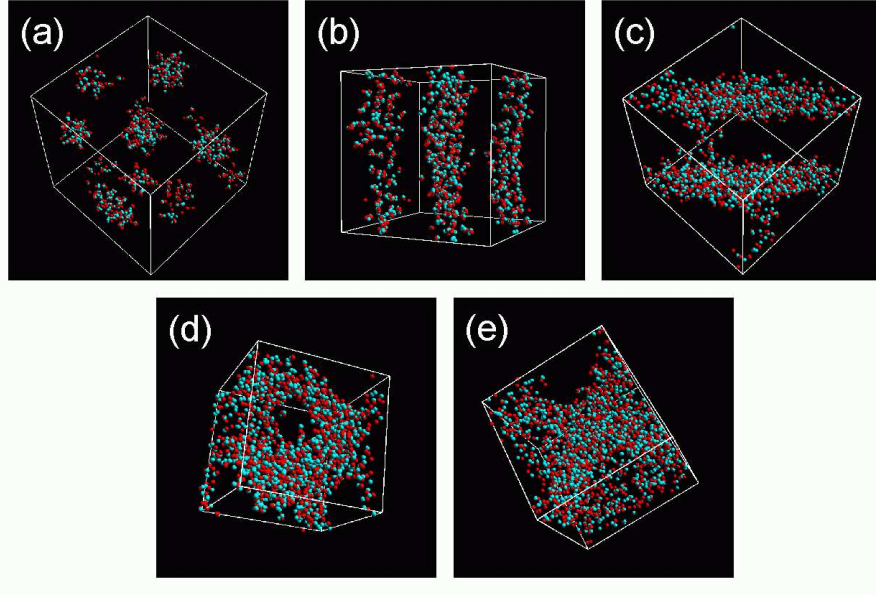


Figure 8: (Color) Nucleon distributions of the pasta phases in cold matter at $x = 0.5$; (a) sphere phase, $0.1\rho_0$ ($L_{\text{box}} = 43.65$ fm, $N = 1372$); (b) cylinder phase, $0.225\rho_0$ ($L_{\text{box}} = 38.07$ fm, $N = 2048$); (c) slab phase, $0.4\rho_0$ ($L_{\text{box}} = 31.42$ fm, $N = 2048$); (d) cylindrical hole phase, $0.5\rho_0$ ($L_{\text{box}} = 29.17$ fm, $N = 2048$) and (e) spherical hole phase, $0.6\rho_0$ ($L_{\text{box}} = 27.45$ fm, $N = 2048$), where L_{box} is the box size and N is the total number of nucleons. The whole simulation box is shown in this figure. The red particles represent protons and the green ones neutrons. Taken from Ref. [68].

snapshots of nucleon distributions at $T = 1, 2$ and 3 MeV for two densities in Figs. 10 and 11. These densities correspond to the phases with rod-like nuclei and with slab-like nuclei at $T = 0$.

From these figures, we can see the following qualitative features (these features are common for $x = 0.5$ and 0.3): at $T \simeq 1.5 - 2$ MeV (but snapshots for $T \simeq 1.5$ MeV are not shown), the number of evaporated nucleons becomes significant; at $T \gtrsim 3$ MeV, nuclei almost melt and the spatial distribution of nucleons are almost smoothed out.

When we try to classify the nuclear structure systematically, the integral mean curvature and the Euler characteristic (a brief explanation is provided in Appendix A) are useful. Here we introduce their normalized quantities: the area-averaged mean curvature $\langle H \rangle$, and the Euler characteristic density χ/V (V is the volume of the whole space). Using a combination of these two quantities calculated for nuclear surface ⁶, each pasta phase can be represented

⁶Nuclear surface generally corresponds to an isodensity surface for the threshold density $\rho_{\text{th}} \simeq 0.5\rho_0$ in our simulations.

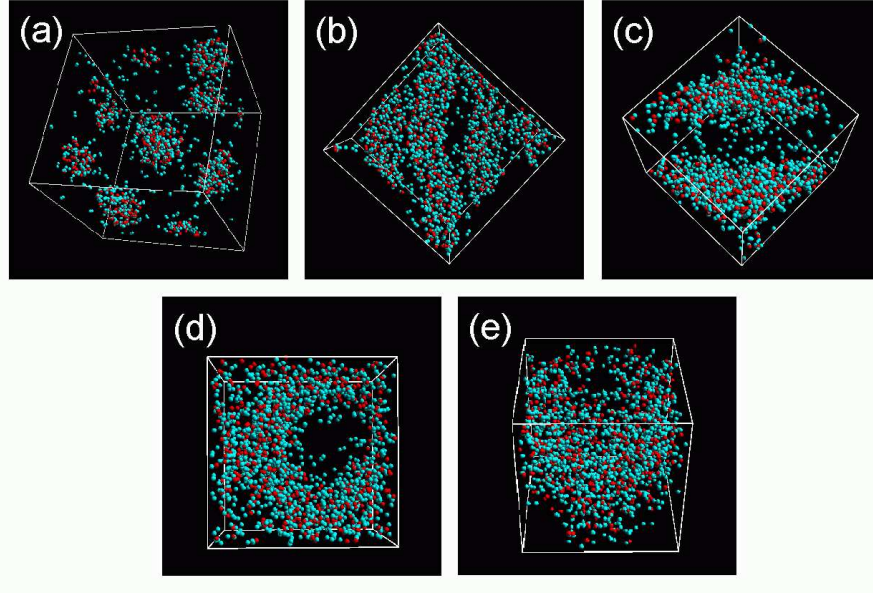


Figure 9: (Color) The same as Fig. 8 at $x = 0.3$; (a) sphere phase, $0.1\rho_0$ ($L_{\text{box}} = 49.88$ fm, $N = 2048$); (b) cylinder phase, $0.18\rho_0$ ($L_{\text{box}} = 41.01$ fm, $N = 2048$); (c) slab phase, $0.35\rho_0$ ($L_{\text{box}} = 32.85$ fm, $N = 2048$); (d) cylindrical hole phase, $0.5\rho_0$ ($L_{\text{box}} = 29.17$ fm, $N = 2048$) and (e) spherical hole phase, $0.55\rho_0$ ($L_{\text{box}} = 28.26$ fm, $N = 2048$). The red particles represent protons and the green ones neutrons. Taken from Ref. [68].

uniquely, i.e.,

$$\text{phase with } \begin{cases} \text{spherical nuclei} & : \langle H \rangle > 0, \chi/V > 0, \\ \text{cylindrical nuclei} & : \langle H \rangle > 0, \chi/V = 0, \\ \text{slab-like nuclei} & : \langle H \rangle = 0, \chi/V = 0, \\ \text{cylindrical bubbles} & : \langle H \rangle < 0, \chi/V = 0, \\ \text{spherical holes} & : \langle H \rangle < 0, \chi/V > 0. \end{cases} \quad (32)$$

We note that the value of χ/V for the ideal pasta phases is zero except for the phase with spherical nuclei or spherical bubbles with positive χ/V ; negative χ/V is not obtained for the pasta phases.

The phase diagrams obtained for $x = 0.5$ and 0.3 are plotted in Figs. 12 and 13, respectively. Qualitative features of these phase diagrams are the same, but the phase separating-region surrounded by a dashed line is smaller for $x = 0.3$ than that for $x = 0.5$. As shown above, nuclear surface can be identified typically at $T \lesssim 3$ MeV (see the dotted lines) in the density range of interest. Thus the regions between the dotted line and the dashed line correspond to some non-uniform phase, which is however difficult to classify into a specific phase because the nuclear surface is hard to identify.

In the region below the dotted lines at $T \lesssim 3$ MeV, where we can identify the nuclear surface, we have obtained the pasta phases with spherical nuclei [region (a)], rod-like nuclei

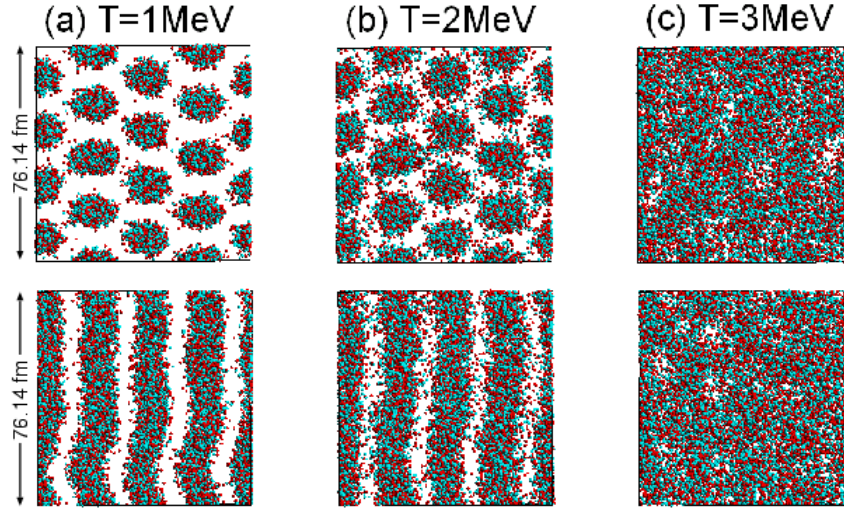


Figure 10: (Color) Nucleon distributions for $x = 0.5$, $\rho = 0.225\rho_0$ at temperatures of 1, 2 and 3 MeV. The total number of nucleons $N = 16384$ and the box size $L_{\text{box}} = 76.14$ fm. The upper panels show top views along the axis of the cylindrical nuclei at $T = 0$, and the lower ones show side views. Protons are represented by the red particles, and neutrons by the green ones. Taken from Ref. [69].

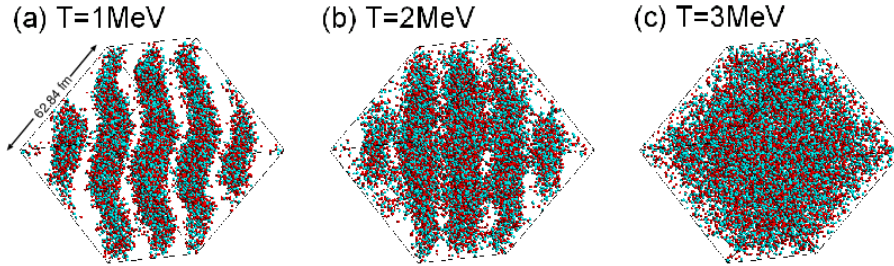


Figure 11: (Color) Nucleon distributions for $x = 0.5$, $\rho = 0.4\rho_0$ at temperatures of 1, 2 and 3 MeV. $N = 16384$ and $L_{\text{box}} = 62.84$ fm. These figures are shown in the direction parallel to the plane of the slab-like nuclei at $T = 0$. Protons are represented by the red particles, and neutrons by the green ones. Taken from Ref. [69].

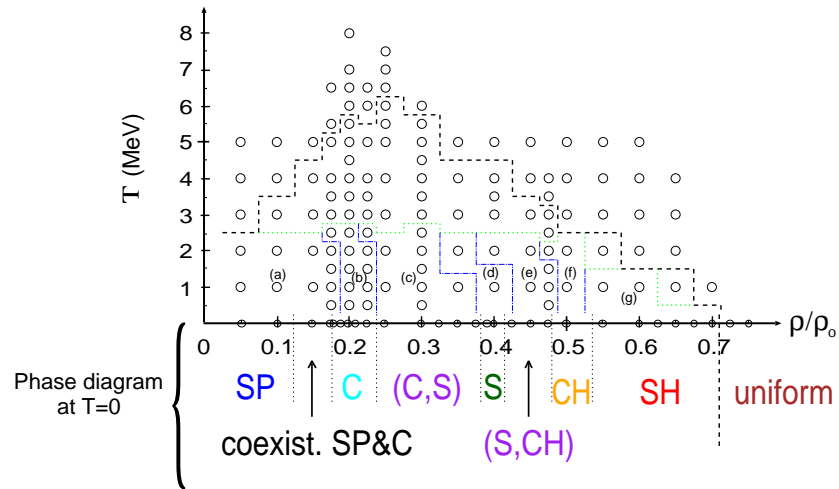


Figure 12: (Color) Phase diagram of matter at $x = 0.5$ plotted in the $\rho - T$ plane. The dashed and the dotted lines on the diagram show the phase separation line and the limit below which the nuclear surface can be identified, respectively. The dash-dotted lines are the phase boundaries between the different nuclear shapes. The symbols SP, C, S, CH, SH, U stand for nuclear shapes, i.e., sphere, cylinder, slab, cylindrical hole, spherical hole and uniform, respectively. The parentheses (A,B) denote an intermediate phase between A and B-phases with a multiply connected structure characterized by negative χ/V . The regions (a)-(g) correspond to the nuclear shapes characterized by $\langle H \rangle$ and χ/V as follows: (a) $\langle H \rangle > 0$, $\chi/V > 0$; (b) $\langle H \rangle > 0$, $\chi/V = 0$; (c) $\langle H \rangle > 0$, $\chi/V < 0$; (d) $\langle H \rangle = 0$, $\chi/V = 0$; (e) $\langle H \rangle < 0$, $\chi/V < 0$; (f) $\langle H \rangle < 0$, $\chi/V = 0$; (g) $\langle H \rangle < 0$, $\chi/V > 0$. Simulations have been carried out at points denoted by circles. Adapted from Ref. [69]

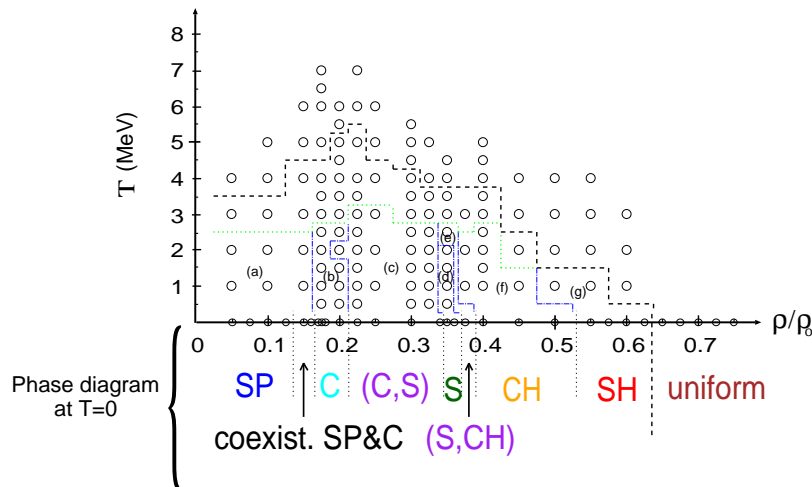


Figure 13: (Color) Phase diagram of matter at $x = 0.3$ plotted in the $\rho - T$ plane. Adapted from Ref. [69].

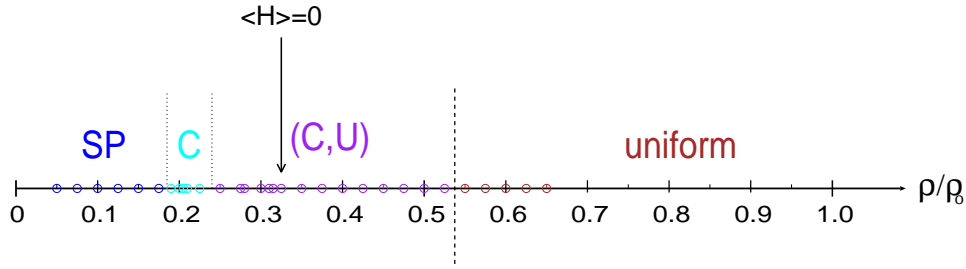


Figure 14: (Color) Phase diagram of cold matter at $x = 0.1$. The density at which the area-averaged mean curvature of nuclear surface is zero is denoted by $\langle H \rangle = 0$ ($\langle H \rangle > 0$ at lower densities than this point and $\langle H \rangle < 0$ at higher densities). However, slab phase is not observed in our results even at this density. Simulations have been carried out at densities denoted by small circles. Adapted from Ref. [68].

[region (b)], slab-like nuclei [region (d)], cylindrical holes [region (f)] and spherical holes [region (g)]. In addition to these pasta phases, structures with negative χ/V have been also obtained in the regions (c) and (e); matter consists of highly connected nuclear and bubble regions (i.e., sponge-like structure) with branching rod-like nuclei, perforated slabs and branching bubbles, etc. A detailed discussion on the phase diagrams is given in Ref. [69]. Effects of the finite box size on the density regions of the phases with negative χ/V should be examined in the future. If these density regions do not decrease significantly even for larger systems, the phases with multiply connected structures would be likely.

We have also investigated cold neutron-rich matter at $x = 0.1$ as a more realistic condition for neutron star matter [68]. The resulting zero-temperature phase diagram is shown in Fig. 14. The pasta phase with rod-like nuclei is obtained around $0.2\rho_0$. A striking feature is that a wide density region from $\sim 0.25\rho_0$ to $\sim 0.525\rho_0$ is occupied by phases with negative χ/V . The structure of matter changes rather continuously from branching rod-like nuclei connected to each other [obtained in the lower density region of the intermediate phase denoted by (C,U)] to branching bubbles connected to each other [higher density region of the intermediate phase (C,U)]. However, in the present neutron-rich case, pasta phase with slab-like nuclei cannot be obtained as far as we have investigated. A further study with a longer relaxation time scale is necessary to determine whether or not the phase with slab-like nuclei is really prohibited in such neutron-rich matter in the present model.

4.3 Structural Transitions between the Pasta Phases

In Ref. [66], we approached the second question asked at the beginning of the present section. We perform QMD simulations of the compression of dense matter and have succeeded in simulating the transitions between rod-like and slab-like nuclei and between slab-like nuclei and cylindrical bubbles.

The initial conditions of the simulations are samples of the columnar phase ($\rho = 0.225\rho_0$) and of the lamellar phase ($\rho = 0.4\rho_0$) with 16384 nucleons at $x = 0.5$ and $T \simeq 1$ MeV. These are obtained in our previous work [69], which are presented in Section 4.2. We then adiabatically compressed the above samples by increasing the density at

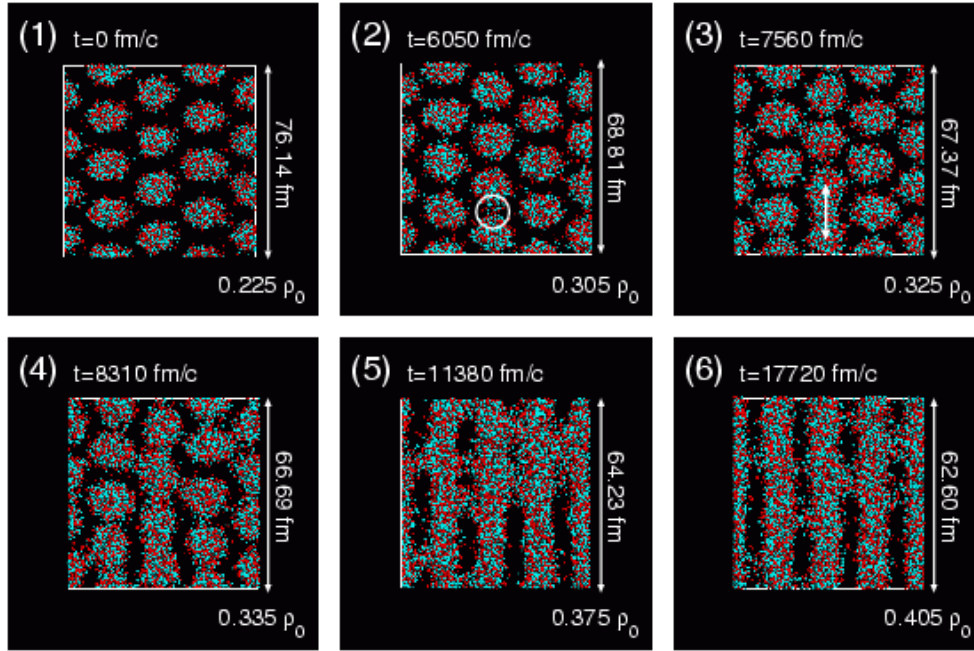


Figure 15: (Color) Snapshots of the transition process from the phase with rod-like nuclei to the phase with slab-like nuclei (the whole simulation box is shown). The red particles show protons and the green ones neutrons. After neighboring nuclei touch as shown by the circle in Fig. 15-(2), the ‘‘compound nucleus’’ elongates along the arrow in Fig. 15-(3). The box size is rescaled to be equal in this figure. Adapted from Ref. [66].

the average rate of $\simeq 1.3 \times 10^{-5} \rho_0 / (\text{fm}/c)$ for the initial condition of the columnar phase and $\simeq 7.1 \times 10^{-6} \rho_0 / (\text{fm}/c)$ for that of the laminar one. According to the typical value of the density difference between each pasta phase, $\sim 0.1 \rho_0$ (see Fig. 12), we increased the density to the value corresponding to the next pasta phase taking the order of $10^4 \text{ fm}/c$. This time scale is much longer than the typical time scale of the deformation and structural transition of nuclei (e.g., that of nuclear fission is $\sim 1000 \text{ fm}/c$). Thus the simulated compression process is adiabatic with respect to the change of nuclear structure, so that the dynamics of the structural transition of nuclei observed in the simulations is physically meaningful, and is essentially independent of the compression rate, etc. Finally, we relaxed the compressed sample at $\rho = 0.405 \rho_0$ for the former case and at $0.490 \rho_0$ for the latter one. These final densities are those of the phase with slab-like nuclei and cylindrical bubbles, respectively, in the equilibrium phase diagram at $T \simeq 1 \text{ MeV}$ (see Fig. 12).

The resulting time evolution of the nucleon distribution is shown in Figs. 15 and 16. As can be seen from Fig. 15, the phase with slab-like nuclei is finally formed [Fig. 15-(6)] from the phase with rod-like nuclei [Fig. 15-(1)]. The temperature in the final state is $\simeq 1.35 \text{ MeV}$. We note that the transition is triggered by thermal fluctuation, not by spontaneous deformation of the rod-like nuclei: when the internuclear spacing becomes small enough and once some pair of neighboring rod-like nuclei touch due to thermal fluctuations, they fuse [Figs. 15-(2) and 15-(3)]. Then such connected pairs of rod-like nuclei further touch

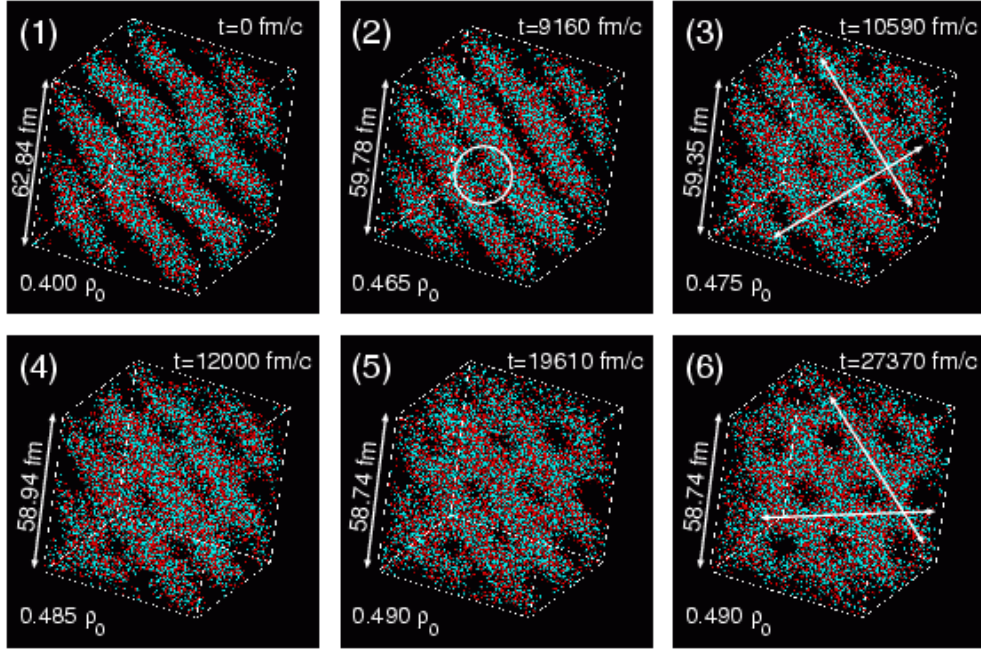


Figure 16: (Color) The same as Fig. 1 for the transition from the phase with slab-like nuclei to the phase with cylindrical holes (the box size is not rescaled in this figure). After the slab-like nuclei begin to touch [see the circle in Fig. 16-(2)], the bridges first crosses them almost orthogonally as shown by the arrows in Fig. 16-(3). Then the cylindrical holes are formed and they relax into a triangular lattice, as shown by the arrows in Fig. 16-(6). Adapted from Ref. [66].

and fuse with neighboring nuclei in the same lattice plane like a chain reaction [Fig. 15-(4)]; the time scale of the each fusion process is of order 10^2 fm/c, which is much smaller than that of the density change.

The transition from the phase with slab-like nuclei to the phase with cylindrical holes is shown in Fig. 16. When the internuclear spacing decreases enough, neighboring slab-like nuclei touch due to the thermal fluctuation as in the above case. Once nuclei begin to touch [Fig. 16-(2)], bridges between the slabs are formed at many places on a time scale (of order 10^2 fm/c) much shorter than that of the compression. After that the bridges cross the slabs almost orthogonally for a while [Fig. 16-(3)]. Nucleons in the slabs continuously flow into the bridges, which become wider and merge together to form cylindrical holes. Afterwards, the connecting regions consisting of the merged bridges move gradually, and the cylindrical holes relax into a triangular lattice [Fig. 16-(6)]. The final temperature in this case is $\simeq 1.3$ MeV.

Trajectories of the above processes on the plane of the integral mean curvature $\int_{\partial R} H dA$ and the Euler characteristic χ are plotted in Fig. 17. This figure shows that the above transitions proceed through a transient state with “sponge-like” structure, which gives negative χ . As can be seen from Fig. 17-(a) [Fig. 17-(b)], the value of the Euler characteristic starts to decrease from zero when the rod-like [slab-like] nuclei touch. It con-

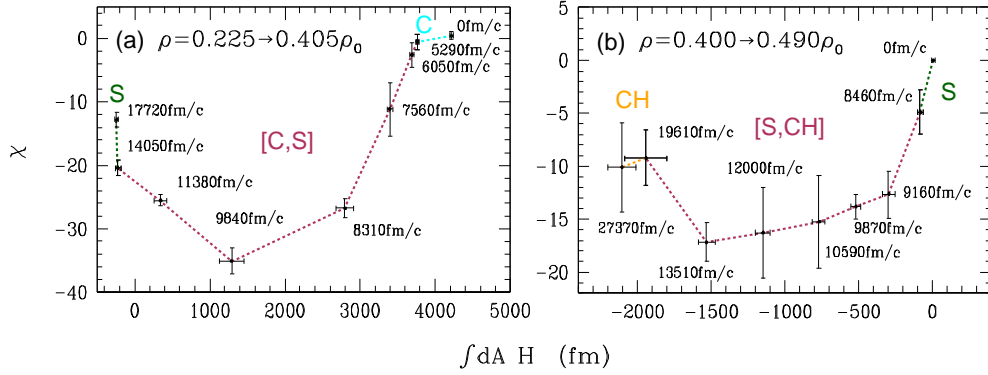


Figure 17: (Color) Time evolution of $\int_{\partial R} HdA$ and χ during the simulations. The data points and the error bars show, respectively, the mean values and the standard deviations in the range of the threshold density (see Appendix A) $\rho_{\text{th}} = 0.3 - 0.5\rho_0$, which includes typical values for the nuclear surface. The panel (a) is for the transition from cylindrical (C) to slab-like nuclei (S) and the panel (b) for the transition from slab-like nuclei to cylindrical holes (CH). Transient states are shown as [C,S] and [S,CH] for each transition. Adapted from Ref. [66].

continues to decrease until all of the rod-like [slab-like] nuclei are connected to others by small bridges at $t \simeq 9840$ fm/c [$\simeq 12000$ fm/c]. Then the bridges merge to form slab-like nuclei [cylindrical holes] and the value of the Euler characteristic increases towards zero. Finally, the system relaxes into a layered lattice of the slab-like nuclei [a triangular lattice of the cylindrical holes]. Thus the whole transition process can be divided into the ‘‘connecting stage’’ and the ‘‘relaxation stage’’ before and after the moment at which the Euler characteristic is minimum; the former starts when the nuclei begin to touch and it takes $\simeq 3000 - 4000$ fm/c and the latter takes more than 8000 fm/c.

4.4 Formation of the Pasta Phases

In closing the present article, let us briefly show our recent results of a study on the formation process of pasta nuclei from spherical ones; i.e., a transition from the phase with spherical nuclei to that with rod-like nuclei. Time evolution of the nucleon distribution in the transition process is shown in Fig. 18. The initial condition of this simulation is a nearly perfect bcc unit cell with 409 nucleons (202 protons and 207 neutrons) at $T \simeq 1$ MeV. We compressed the system in a similar way to that of the simulations explained in Section 4.3. The average rate of the density change in the present case is $\simeq 4.4 \times 10^{-6} \rho_0 / (\text{fm}/c)$. Since the two nuclei start to touch [see the circles in Fig. 18-(2)], the transition process completes within $\simeq 2500$ fm/c and the rod-like nucleus is formed. The final state [Fig. 18-(4)] is a triangular lattice of the rod-like nuclei.

The present simulation has been performed using a small system; effects of the finite system size in this simulation should be examined. Detailed investigation of the transition using a larger system will be presented in a future publication [61].

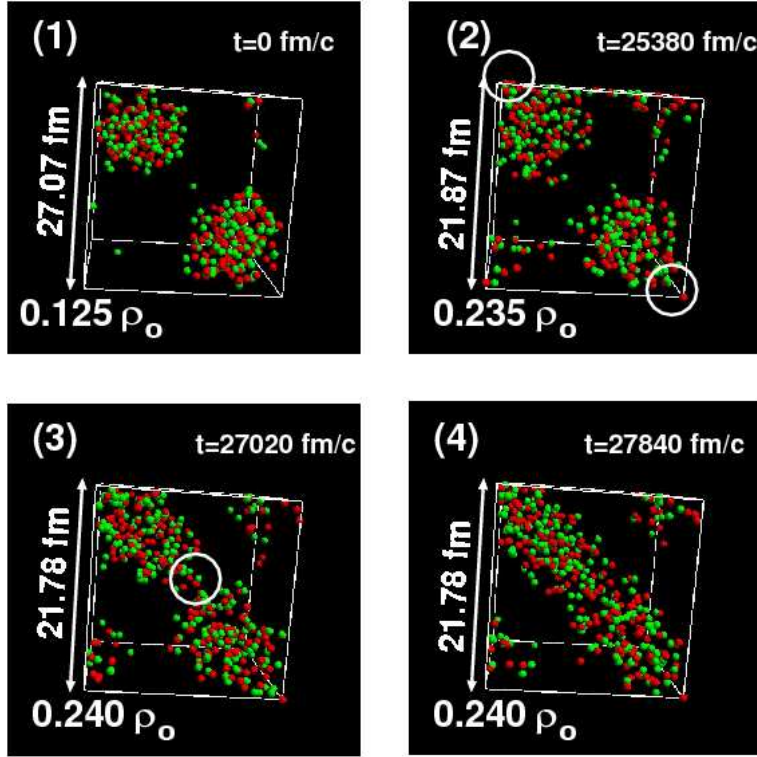


Figure 18: (Color) Snapshots of the transition process from the bcc lattice of spherical nuclei to the triangular lattice of rod-like nuclei (the whole simulation box is shown). The red particles show protons and the green ones neutrons. The box size is rescaled to be equal in this figure.

5 Summary

In this article, we have explained the basic physics and astrophysics of non-spherical nuclei, nuclear pasta, in compact objects. In supernova cores and neutron stars, density can be very high; when the density approaches that of atomic nuclei, the Coulomb force starts to matter and to compete against the surface tension of nuclei. Exotic nuclear shapes result from the competition between these two opposite effects. The presence of the pasta phases would affect various astrophysical phenomena. Especially, impacts on the neutrino opacity of collapsing stellar cores should be examined in the near future.

We have discussed the similarity between the pasta phases and soft condensed matter systems. Pasta phases with rod-like nuclei and slab-like nuclei have similar elastic properties to those of some phases of liquid crystals: columnar phase and smectic A phase, respectively. With the help of this concept, thermodynamic stability of the phase with slab-like nuclei and melting temperature of the phase with rod-like nuclei have been discussed.

Nuclear systems can be regarded as complex fluids of nucleons and their nature of a complex fluid sets limits on the validity of methods commonly used in previous studies of pasta phases. However, a gap between the typical length scale of the semimacroscopic

pasta phases and that of the nucleon is not large. Due to this small gap, we can study pasta phases using some microscopic approach: the quantum molecular dynamics (QMD) is one possibility.

We have explained the theoretical framework of molecular dynamics calculations for nucleons including QMD and then given an overview of our previous work. Our QMD simulations have shown that the pasta phases can be formed dynamically by cooling down hot uniform nuclear matter in a finite time scale $\sim O(10^3 - 10^4)$ fm/ c , which is much shorter than the cooling time of a neutron star. We have also shown that transitions between the pasta phases can occur by compression during the collapse of a star. Our latest result strongly suggests that the pasta phase with rod-like nuclei can be formed by compressing a bcc lattice of spherical nuclei; this result will be examined in detail.

As we have shown, nuclear pasta is an interesting system for a wide spectrum of researchers not only to nuclear astrophysicists. Physics of the pasta phases draws on nuclear physics, condensed matter physics, and astrophysics. The pasta phases are important for understanding stellar collapse and neutron star formation, which are long-standing mystery in the Universe.

Acknowledgements

The authors are grateful to Kazuhiro Oyamatsu for giving us permission to use Fig. 3. They also thank Chris Pethick for helpful comments. The research reported in this article grew out of collaborations with Kei Iida, Toshiki Maruyama, Katsuhiko Sato, Kenji Yasuoka and Toshikazu Ebisuzaki. Further research currently in progress is performed using the RIKEN Super Combined Cluster System with MDGRAPE-2. This work was supported in part by the Nishina Memorial Foundation, by a JSPS Postdoctoral Fellowship for Research Abroad, by a JSPS Research Fellowship for Young Scientists, by the Ministry of Education, Culture, Sports, Science and Technology through Research Grant No. 14-7939, and by RIKEN through Research Grant No. J130026.

A The Integral Mean Curvature and the Euler Characteristic

The integral mean curvature and the Euler characteristic (see, e.g., Ref. [39] and references therein for details) are powerful tools for extracting the morphological characteristics of the structure of nuclear matter. Suppose there is a set of regions R , where the density is higher than a given threshold density ρ_{th} . The integral mean curvature and the Euler characteristic for the surface of this region ∂R are defined as surface integrals of the mean curvature $H = (\kappa_1 + \kappa_2)/2$ and the Gaussian curvature $G = \kappa_1\kappa_2$, respectively; i.e., $\int_{\partial R} H dA$ and $\chi \equiv \int_{\partial R} G dA/2\pi$, where κ_1 and κ_2 are the principal curvatures and dA is the area element of the surface of R . The Euler characteristic χ depends only on the topology of R and is expressed as

$$\chi = (\text{number of isolated regions}) - (\text{number of tunnels}) + (\text{number of cavities}) . \quad (33)$$

Their normalized quantities, the area-averaged mean curvature $\langle H \rangle$ and the Euler characteristic density are also useful. They are defined as $\langle H \rangle \equiv A^{-1} \int H dA$, and χ/V , respectively, where V is the volume of the whole space.

According to Eq. (33), sphere and spherical holes give $\chi > 0$; infinitely long rods, infinitely extending slabs and infinitely long cylindrical holes give $\chi = 0$. Multiply connected structures such as “sponge” give negative χ .

References

- [1] J. Aichelin, *Phys. Rep.* **202** (1991) 233.
- [2] J. Aichelin and H. Stöcker, *Phys. Lett.* **B176** (1986) 14.
- [3] M. P. Allen and D. J. Tildesley, *Computer Simulation of Liquids* (Clarendon, Oxford, 1987).
- [4] P. W. Anderson and N. Itoh, *Nature* **256** (1975) 25.
- [5] G. Baym, H. A. Bethe and C. J. Pethick, *Nucl. Phys.* **A175** (1971) 225.
- [6] H. A. Bethe, *Rev. Mod. Phys.* **62** (1990) 801.
- [7] H. A. Bethe, G. Börner and K. Sato, *Astron. and Astrophys.* **7** (1970) 279.
- [8] P. Bonche and D. Vautherin, *Nucl. Phys.* **A372** (1981) 496.
- [9] A. Burrows, S. Reddy and T. A. Thompson, *Nucl. Phys.* **A777** (2006) 356.
- [10] N. Chamel, *Nucl. Phys.* **A747** (2005) 109.
- [11] S. Chandrasekhar, *Liquid Crystals, 2nd ed.* (Cambridge Univ. Press, Cambridge, 1992).
- [12] S. A. Colgate and R. H. White, *Astrophys. J.* **143** (1966) 626.
- [13] P. G. de Gennes and J. Prost, *The Physics of Liquid Crystals, 2nd ed.* (Clarendon, Oxford, 1993).
- [14] H. Feldmeier, *Nucl. Phys.* **A515** (1990) 147.
- [15] H. Feldmeier and J. Schnack, *Prog. Part. Nucl. Phys.* **39** (1997) 393.
- [16] H. Feldmeier and J. Schnack, *Rev. Mod. Phys.* **72** (2000) 655.
- [17] D. Z. Freedman, *Phys. Rev. D* **9** (1974) 1389.
- [18] D. Z. Freedman, D. N. Schramm and D. L. Tubbs, *Annu. Rev. Nucl. Sci.* **27** (1977) 167.
- [19] D. Frenkel and B. Smit, *Understanding Molecular Simulation* (Academic Press, London, 1996).
- [20] M. Hashimoto, H. Seki and M. Yamada, *Prog. Theor. Phys.* **71** (1984) 320.
- [21] H. Heiselberg and M. Hjorth-Jensen *Phys. Rep.* **328** (2000) 237.

-
- [22] C. J. Horowitz, M. A. Pérez-García and J. Piekarewicz, *Phys. Rev. C* **69** (2004) 045804.
- [23] C. J. Horowitz, M. A. Pérez-García, J. Carriere, D. K. Berry and J. Piekarewicz, *Phys. Rev. C* **70**, 065806 (2004).
- [24] K. Iida, G. Watanabe and K. Sato, *Prog. Theor. Phys.* **106** (2001) 551; Erratum, *Prog. Theor. Phys.* **110** (2003) 847.
- [25] H.-Th. Janka, K. Langanke, A. Marek, G. Martínez-Pinedo, and B. Müller, *Phys. Rep.* **442** (2007) 38.
- [26] P. B. Jones, *Mon. Not. R. Astron. Soc.* **296** (1998) 217; *Mon. Not. R. Astron. Soc.* **306** (1998) 327; *Phys. Rev. Lett.* **83** (1999) 3589.
- [27] A. D. Kaminker, C. J. Pethick, A. Y. Potekhin, V. Thorsson and D. G. Yakovlev, *Astron. and Astrophys.* **343** (1999) 1009.
- [28] T. Kawakatsu, Y. Yamazaki and M. Imura, *Bussei Kenkyu* **74** (1999) 555 (in Japanese).
- [29] T. Kido, T. Maruyama, K. Niita and S. Chiba, *Nucl. Phys.* **A663 & 664** (2000) 877c.
- [30] D. Q. Lamb, J. M. Lattimer, C. J. Pethick and D. G. Ravenhall, *Phys. Rev. Lett.* **41** (1978) 1623.
- [31] L. D. Landau and E. M. Lifshitz, *Statistical Physics, 3rd ed.* (Pergamon, New York, 1980).
- [32] M. Lassaut, H. Flocard, P. Bonche, P. -H. Heenen and E. Suraud, *Astron. Astrophys.* **183** (1987) L3.
- [33] J. M. Lattimer and M. Prakash, *Science* **304** (2004) 536.
- [34] C. P. Lorenz, D. G. Ravenhall and C. J. Pethick, *Phys. Rev. Lett.* **70** (1993) 379.
- [35] P. Magierski and P. -H. Heenen, *Phys. Rev. C* **65** (2002) 045804.
- [36] G. Martínez-Pinedo, M. Liebendörfer, D. Frekers, *Nucl. Phys.* **A777** (2006) 395.
- [37] T. Maruyama, K. Niita, K. Oyamatsu, T. Maruyama, S. Chiba and A. Iwamoto, *Phys. Rev. C* **57** (1998) 655.
- [38] T. Maruyama, D. N. Voskresensky, T. Tanigawa and S. Chiba, *Phys. Rev. C* **72** (2005) 015802.
- [39] K. Michielsen and H. De Raedt, *Phys. Rep.* **347** (2001) 461.
- [40] J. W. Negele and D. Vautherin, *Nucl. Phys.* **A207** (1973) 298.
- [41] K. Niita, in the Proceedings of the Third Symposium on “*Simulation of Hadronic Many-body System*”, A. Iwamoto *et al.*, Eds., JAERI-conf. 96-009 (1996) 22 (in Japanese).

-
- [42] A. Ohnishi and J. Randrup, *Phys. Rev. Lett.* **75** (1995) 596; *Phys. Rev. A* **55** (1997) 3315(R).
- [43] E. Olsson, Master Thesis, Uppsala University (1999).
- [44] A. Ono, H. Horiuchi, T. Maruyama and A. Ohnishi, *Prog. Theor. Phys.* **87** (1992) 1185; *Phys. Rev. Lett.* **68** (1992) 2898.
- [45] K. Oyamatsu, *Nucl. Phys.* **A561** (1993) 431.
- [46] K. Oyamatsu, PhD thesis, Waseda University (1994).
- [47] K. Oyamatsu, M. Hashimoto and M. Yamada, *Prog. Theor. Phys.* **72** (1984) 373.
- [48] K. Oyamatsu and M. Yamada, *Nucl. Phys.* **A578** (1994) 181.
- [49] C. J. Pethick and A. Y. Potekhin, *Phys. Lett.* **B427** (1998) 7.
- [50] C. J. Pethick and D. G. Ravenhall, *Annu. Rev. Nucl. Part. Sci.* **45** (1995) 429.
- [51] C. J. Pethick and V. Thorsson, *Phys. Rev. Lett.* **72** (1994) 1964; *Phys. Rev. D* **56** (1997) 7548.
- [52] D. G. Ravenhall, C. D. Bennett and C. J. Pethick, *Phys. Rev. Lett.* **28** (1972) 978.
- [53] D. G. Ravenhall, C. J. Pethick and J. R. Wilson, *Phys. Rev. Lett.* **50** (1983) 2066.
- [54] M. Ruderman, *Nature* **223** (1969) 597.
- [55] K. Sato, *Prog. Theor. Phys.* **53** (1975) 595; *Prog. Theor. Phys.* **54** (1975) 1325.
- [56] K. Sato, in the proceedings of the 1st Yamada Symposium on the “*Neutrinos and Dark Matter in Nuclear Physics*”,
http://ndm03.phys.sci.osaka-u.ac.jp/presentations/Session_VIII/K_Sato.pdf.
- [57] S. L. Shapiro and S. A. Teukolsky, *Black Holes, White Dwarfs, and Neutron Stars* (Wiley, New York, 1983).
- [58] H. Sonoda, G. Watanabe, K. Sato, T. Takiwaki, K. Yasuoka and T. Ebisuzaki, *Phys. Rev. C* **75** (2007) 042801(R).
- [59] K. Sumiyoshi, K. Oyamatsu and H. Toki, *Nucl. Phys.* **A595** (1995) 327.
- [60] H. Suzuki, in: M. Fukugita and A. Suzuki (Eds.), *Physics and Astrophysics of Neutrinos* (Springer, Tokyo, 1994) p. 763.
- [61] G. Watanabe, H. Sonoda, T. Maruyama, K. Sato, K. Yasuoka and T. Ebisuzaki, in preparation.
- [62] G. Watanabe, in the Proceedings of the Tours Symposium on Nuclear Physics VI, *AIP Conf. Proc.* **891** (2007) 373 (nucl-th/0610116).
- [63] G. Watanabe and K. Iida, *Phys. Rev. C* **68** (2003) 045801.

-
- [64] G. Watanabe, K. Iida and K. Sato, *Nucl. Phys.* **A676** (2000) 455; Erratum, *Nucl. Phys.* **A726** (2003) 357.
- [65] G. Watanabe, K. Iida and K. Sato, *Nucl. Phys.* **A687** (2001) 512; Erratum, *Nucl. Phys.* **A726** (2003) 357.
- [66] G. Watanabe, T. Maruyama, K. Sato, K. Yasuoka and T. Ebisuzaki, *Phys. Rev. Lett.* **94** (2005) 031101.
- [67] G. Watanabe, K. Sato, K. Yasuoka and T. Ebisuzaki, *Phys. Rev. C* **66** (2002) 012801(R).
- [68] G. Watanabe, K. Sato, K. Yasuoka and T. Ebisuzaki, *Phys. Rev. C* **68** (2003) 035806.
- [69] G. Watanabe, K. Sato, K. Yasuoka and T. Ebisuzaki, *Phys. Rev. C* **69** (2004) 055805.
- [70] R. D. Williams and S. E. Koonin, *Nucl. Phys.* **A435** (1985) 844.
- [71] J. R. Wilson, in: J. M. Centrella *et al.* (Eds.), *Numerical Astrophysics* (Jones and Bartlett Publ., Portola Valley, 1985) p. 422.
- [72] S. E. Woosley, A. Heger and T. A. Weaver, *Rev. Mod. Phys.* **74** (2002) 1015.
- [73] S. E. Woosley and T. -H. Janka, *Nature Physics* **1** (2005) 147.
- [74] D. G. Yakovlev and C. J. Pethick, *Ann. Rev. Astron. Astrophys.* **42** (2004) 169.